Near-Field Control and Imaging of Free Charge Carrier Variations in GaN Nanowires

Samuel Berweger,

Paul T. Blanchard,

Matt D. Brubaker,

Kevin J. Coakley,

Norman A. Sanford,

Thomas M. Wallis,

Kris A. Bertness,

Pavel Kabos

National Institute of Standards and Technology, Boulder, CO, 80305

Abstract

Despite their uniform crystallinity, the shape and faceting of semiconducting nanowires (NWs) can give rise to variations in structure and associated electronic properties. Here we develop a hybrid scanning probe-based methodology to investigate local variations in electronic structure across individual n-doped GaN NWs integrated into a transistor device. We perform scanning microwave microscopy (SMM), which we combine with scanning gate microscopy (SGM) to determine the free-carrier SMM signal contribution and image local charge carrier density variations. In particular, we find significant variations in free carriers across NWs, with a higher carrier density at the wire facets. By increasing the local carrier density through tip-gating, we find that the tip injects current into the NW with strongly localized current when positioned over the wire vertices. These results suggest that the strong variations in electronic properties observed within NWs have significant implications for device design and may lead to new paths to optimization.

Low-dimensional semiconducting materials are attractive for novel electronic and optoelectronic applications [1, 2] due to their inherently small size and tunable material properties [3, 4]. 1D nanowires (NWs) can achieve particularly high crystal quality using established growth methods [5, 6]. Although NWs are widely used for hybrid devices [7, 8], the control of doping and morphology even enables monolithic functional devices within single crystal NWs [9, 10] that can eliminate practical challenges and limitations due to material heterojunctions. NWs can nevertheless exhibit both radial and azimuthal variations in electronic properties due to effects such as strain [11], surface traps [12], or compositional variations [13, 14]. Thus, although they are often approximated as idealized uniform cylinders, NWs exhibit complex behavior even transversely across a single wire, which is expected to affect characteristics such as transport and carrier injection that fundamentally underpin device performance.

The electrically enabled variants of atomic force microscopy (AFM) can probe sample electronic properties with the nanometer spatial resolution necessary to study variations

within single wires. These techniques include scanning gate microscopy (SGM) [15, 16], conductive AFM (c-AFM) [17–19], Kelvin probe force microscopy (KPFM) [20, 21], and scanning microwave microscopy (SMM) [22–30]. While these techniques have been individually applied to NWs [16, 18, 20, 21, 24], they often provide only an incomplete picture of sample properties. SMM in particular can measure free charge carriers [24–26], but suffers from a host of artifacts and spurious signals including the stray capacitance [27, 28] and a possible water meniscus [29]. While the signal contribution of interest can often be identified using finite element modeling [23, 25, 28] or careful calibration [27, 30], this is often time-consuming and difficult.

Here we present a hybrid scanning probe methodology that leverages the complementary information obtained from SMM, SGM, and c-AFM to study electronic variations across individual semiconducting n-doped GaN NWs in a transistor architecture. We use the source-drain NW current measured while reverse-biasing the tip-NW Schottky junction to identify the SMM signal contribution from the free carriers. Using the free carrier-based SMM signal together with the spatially varying NW current we confirm the reduced charge carrier concentration at the wire vertices. We further find that forward-biasing the junction results in strongly localized current injection with the tip located at the wire vertices.

Single crystal c-axis GaN NWs were grown by plasma-assisted molecular beam epitaxy [31] with Si doping to a carrier concentration of $n_e = (2.5 \pm 0.3) \times 10^{17}$ cm^{-3} [32]. n-type NW devices with ohmic contact [33] are fabricated by photolithography as described previously [9]. An optical micrograph of the NW device studied here is shown in Fig. 1(a) and the corresponding current-voltage (*I-V*) curve is shown in Fig. 1(b). A high-resolution scanning electron micrograph (SEM) of the same wire is shown in Fig. 1(c), showing the hexagonal NW shape with a top facet width of (66 ±5) nm corresponding to a typical diameter of ~120 nm.

The combined SMM and SGM instrument, shown schematically in Fig. 1(d), is based on a commercial AFM operating in contact mode under ambient conditions as described elsewhere [24, 25]. We measure the uncalibrated reflected S_{11} signal, where the operating frequency of 18.78 GHz is chosen to maximize the NW signal. The S_{11} signal probes the local dielectric environment [24, 28], including the free carrier (Drude) contribution [26] to the NW dielectric function $\epsilon_{\text{GaN}} = \epsilon_{\infty} + \epsilon_{\text{D}}$. The tip bias V_t is used to locally gate the wire while the grounded global backgate $V_{\text{BG}} = 0$ V ensures an otherwise uniform wire carrier density. The wire current I_{NW} at the drain electrode is acquired concurrently with the AFM topography and S_{11} signal.

While this work describes results obtained from the wire shown in Fig. 1(a–c), these results are consistent across four different wire devices measured. Shown in Fig. 1 is the contact-mode AFM topography (e) and S_{11} signal (f) from the NW device, with the contact electrodes immediately outside the field of view. The wire thickness of 118 nm is as expected and the topographic deviation from the ideal hexagonal shape is due to convolution of the wire cross-section with the AFM tip shape. While both the topography and S_{11} image show little change along the length of the wire, the S_{11} image shows significant lateral variations across the wire.

In order to understand the origin of the S_{11} signal variations across the wire and identify the free carrier contributions, we perform SGM concurrently with SMM and repeatedly scan across the wire at the position marked by the dashed line in Fig. 1(e–f). Illustrated in Fig. 2(a) is the radial electronic structure of n-type NWs with the expected effects of the tip bias as indicated. Due to surface traps [12, 34] and strain [20], the GaN bands bend upward near the surface. This band bending leads to carrier depletion at the surface with the majority of longitudinal carrier transport occurring near the core, and the surface pinning ensures a tip-GaN Schottky barrier. A reverse bias ($V_t < 0$) then increases the upward band bending at the surface, further increases its penetration into the wire bulk, and is thus expected to reduce the local carrier density and the associated NW current. Conversely, a forward bias ($V_t > 0$) is expected to reduce the local barrier height and increase the local conductivity.

The absolute source-drain current I_{NW} in response to reverse biasing the Schottky barrier, measured during scanning with the tip on the center facet of the NW, is shown in Fig. 2(b). As expected, decreasing V_t (more negative, blue) reduces the current with full local carrier depletion seen when the wire ceases to conduct at $V_t = -5$ V. The behavior is reversed as the carriers accumulate again when V_t is increased (returning to neutral, red), though a hysteresis is seen that arises from the long-term kinetics related to the activation and passivation of surface trap states [12].

Shown in Fig. 2(c) are the corresponding line cuts of the SMM signal across the wire acquired with intrinsic doping (blue) and fully depleted (cyan). As only the tip bias is changed between these two scans, the difference in S_{11} between these two line cuts (red) results only from the change in free carrier density. Therefore we subtract the SMM signal obtained from the locally depleted NW to correct for artifacts, including the stray capacitance and possible water meniscus, which are expected to be unchanged. We denoise all further S_{11} scans with an Adaptive Weights Smoothing method that maintains sharp spatial features while removing noise [35]. We note that the S_{11} signal is not expected to be linear with carrier density, and our uncalibrated SMM results provide only a qualitative measure of the carrier distribution.

The tip bias-dependent evolution of the free carrier contribution to the SMM signal across the NW is shown in Fig. 2(d) with the NW edges indicated by dotted lines. The signal shows a clear dependence on the tip bias, further confirming the signal origin from the free carriers. A strong increase in signal is seen with the tip above the wire facets, with a decrease in signal seen with the tip positioned over the vertices (dashed lines in Fig. 2(c)). These signal variations suggest a nonuniform free carrier concentration. Although the wire is expected to be highly symmetric and we ensure sharp tips, some asymmetry is nevertheless seen in the gating response and S_{11} signal across the wire.

We further investigate the electronic properties of the NW vertices through the spatially varying bias-dependent NW current. Shown in Fig. 2(e) is the corresponding V_t-dependent spatially resolved change in wire current I_{NW}, where the corresponding I_{NW} with the tip away from the wire has been subtracted from each line. With increasing V_t magnitude strong spatial variations in I_{NW} are seen as a result of changes in gating efficacy across the wire, where the large capacitive interaction area with the tip adjacent to the NW leads to a

strong gating response. For $V_t = -5$ V the wire ceases to conduct and due to hysteresis (see supplement [36]) does not recover even with the tip away from the wire.

Shown in Fig. 2(e) is a line cut for I_{NW} (green) for $V_t = -2$ V and the corresponding AFM topography (black). Dashed lines show the position of the wire vertices as estimated from the SEM micrograph. Similar to the reduced S_{11} signal at the wire vertices (Fig. 2(c)), a small decrease in the wire gating response is seen here.

Further notable effects are seen at the NW vertices when the tip-NW schottky barrier is forward-biased. As the current is the result of the integrated resistivity along the length of the wire, a spatially localized increase in carrier density and the associated decrease in resistivity due to positive V_t is not expected to significantly decrease the total wire resistance. Fig. 2(g) shows I with an applied tip bias of 1 V, where the wire current nevertheless increases to values approximately three times the baseline amount with the tip at the wire vertices, and a small amount is seen with the tip over the facets. The forward bias on the Schottky junction thus reduces the band bending, which allows electrons to flow from the GaN conduction band to the tip and creates a net positive current from the tip to the wire that is summed with the source-drain current.

These results emphasize notable differences in electronic properties and free-charge carrier density between the wire vertices and the facets. In particular, the reduced free carrier S_{11} signal and the reduced gating efficacy confirm the larger surface band bending and resulting reduced carrier density at the vertices [20]. However, the larger band bending and associated injection barrier at the wire vertices would suggest current should flow predominantly at the facets and not at the vertices as observed.

This increased current injection can occur due to either the strong local fields generated at the tip-facet gap reducing the schottky barrier height $\Delta\Phi \propto \sqrt{E}$, or the tip pressure penetrating through the surface adsorbates or possible oxide layer [19]. However, we maintain a tip-sample force of < 200 nN and see no degradation of the soft Pt tip that would suggest the strong pressure necessary to penetrate a surface oxide. We further note that although the tip force on the side facet is perpendicular to the facet normal, increased current injection is nevertheless observed, suggesting field enhancement as the dominant barrier-lowering mechanism. As the field enhancement is expected to be stronger at the top wire vertices that are oriented along the tip axis compared to the lateral side facets, the higher injection current at the top facets further supports this conclusion.

The capability of SMM to directly detect free charge carriers is unique for scanning probe methodologies, and while data interpretation is often difficult, the independent control of the DC or low-frequency tip bias allows for complementary parallel measurements such as SGM or c-AFM as demonstrated here. In particular, in addition to obtaining complimentary information from these additional implementations, they can also be used for background subtraction and signal correction. This hybrid methodology presents a new approach that not only enables the imaging of free carriers, but can also simultaneously control their density via independent approaches including optical carrier injection (see supplement [36]).

While sophisticated growth techniques allow for a high degree of morphological control of semiconducting NWs, the polygonal cross-sections can result in spatially varying electronic properties. Importantly, we observe notable differences between wire facets and vertices. The reduction in the tip gating efficacy together with the S_{11} signal at the vertices confirms previous work identifying increased band bending at the wire vertices and a resulting local decrease in carrier concentration and conductivity [12, 20]. Furthermore, the sharp aspect of the facets makes these susceptible to pressure- and field-dependent effects that can significantly impact local electrical performance and applied contacts.

Here we have studied lateral variations in electronic structure and free carrier concentration in single crystal GaN NWs using a hybrid scanning probe technique. This technique combines microwave near-field imaging with local tip gating and conductive AFM, and allows for the imaging of the wire carrier density using the microwave signal while simultaneously and independently controlling it using a DC bias. In particular, we use local gating and depletion of the NW free carriers to identify the free carrier contribution to the S_{11} signal while also providing complementary spatially resolved information. We identify significant differences in electronic properties between the NW facets and vertices, and confirm that the hexagonal cross-section leads to increased surface band bending at the wire vertices. We further measure increased current injection at the vertices, which has significant implications for device contacts. This suggests that beyond simple approximations of 1D wires as round structures, device design and optimization requires consideration of the actual cross-sectional shape.

We would like to thank Benjamin Klein for insightful discussions.

Supplementary Material

Refer to Web version on PubMed Central for supplementary material.

References

[1]. Appenzeller J, Knoch J, Björk MT, Riel H, Schmid H, and Riess W, IEEE Trans. Electron. Dev 55, 2827 (2008).

[2]. Franklin AD, Science 349, aab2750 (2015).

[3]. Wang QH, Kalantar-Zadeh K, Kis A, Coleman JN, and Strano MS, Nat. Nanotech 7, 699 (2012).

[4]. Wang Y and Herron N, J. Phys. Chem 95, 525 (1991).

[5]. Bertness KA, Roshko A, Sanford NA, Barker JM, and Davydov A, J. Cryst. Growth 287, 522 (2006).

[6]. Wu Y, Cui Y, Huynh L, Barrelet CJ, Bell DC, and Lieber CM, Nano Lett. 4, 433 (2004).

[7]. Oulton RF, Sorger VJ, Zentgraf T, Ma R-M, Gladden C, Dai L, Bartal G, and Zhang X, Nature 461, 629 (2009). [PubMed: 19718019]

[8]. Garnett EC, Brongersma ML, Cui Y, and McGhee MD, Ann. Rev. Mater. Res 41, 269 (2011).

[9]. Brubaker MD, Blanchard PT, Schlager JB, Sanders AW, Roshko A, Duff SM, Gray JM, Bright VM, Sanford NA, and Bertness KA, Nano Lett. 13, 347 (2013).

[10]. Christesen JD, Zhang X, Pinion CW, Celano TA, Flynn CJ, and Cahoon JF, Nano Lett. 12, 6024 (2012). [PubMed: 23066872]

[11]. Zhu Z, Zhang A, Ouyang G, and Yang G, Appl. Phys. Lett 98, 263112 (2011).

[12]. Sanford NA, Blanchard PT, Bertness KA, Mans-field L, Schlager JB, Sanders AW, Roshko A, Burton BB, and George SM, J. Appl. Phys 107, 034318 (2010).

[13]. Heiss M, Fontana Y, Gustafsson A, Wst G, Magen C, ORegan DD, Luo JW, Ketterer B, Conesa-Boj S, Kuhlmann AV, Houel J, Russo-Averchi E, Morante JR, Cantoni M, Marzari N, Arbiol J, Zunger A, Warburton RJ, and Fontcuberta i Morral A, Nat. Mater 12, 439 (2013). [PubMed: 23377293]

[14]. Fang Z, Robin E, Rozas-Jiménez E, Cros A, Donatini F, Mollard N, Pernot J, and Daudin B, Nano Let 15, 6794 (2015). [PubMed: 26426262]

[15]. Eriksson MA, Beck RG, Topinka M, Katine JA, Westevelt RM, Campman KL, and Gossard AC, Appl. Phys. Lett 69, 671 (1996).

[16]. Zhou X, Dayeh SA, Wang D, and Yu ET, Appl. Phys. Lett 90, 233118 (2007).

[17]. Zhang L, Sakai T, Sakuma N, and Nakayama TOK, Appl. Phys. Lett 75, 3527 (1999).

[18]. Cheng G, Wang S, Cheng K, Jiang X, Wang L, Li L, Du Z, and Zou G, Appl. Phys. Lett 92, 223116 (2008).

[19]. Brezna W and Smoliner J, J. A (2008).

[20]. Henning A, Klein B, Bertness KA, Blanchard PT, Sanford NA, and Rosenwaks Y, J. Appl. Phys 105, 213107 (2014).

[21]. Koren E, Berkovitch N, Azriel O, Boag A, Rosenwaks Y, Hemesath ER, and Lauhon LJ, Appl. Phys. Lett 99, 223511 (2011).

[22]. Fee M, Chu S, and Hänsch TW, Opt. Commun 69, 219 (1989).

[23]. Kundhikanjana W, Lai K, Wang H, Dai H, Kelly MA, and Shen ZX, Nano Lett. 9, 3762 (2009). [PubMed: 19678669]

[24]. Imtiaz A, Wallis TM, Weber JC, Coakley KJ, Brubaker MD, Blanchard PT, Bertness KA, Sanford NA, and Kabos P, Appl. Phys. Lett 104, 263107 (2014).

[25]. Berweger S, Weber JC, John J, Velazquez JM, Pieterick A, Sanford NA, Davydov AV, Brunschwig B, Lewis NS, Wallis TM, and Kabos P, Nano Lett. 15, 1122 (2015). [PubMed: 25625509]

[26]. Imtiaz A, Wallis TM, Lim SH, Tanbakuchi H, Huber HP, Hornung A, Hinterdorfer P, Smoliner J, Kienberger F, and Kabos P, J. Appl. Phys 111, 093727 (2012).

[27]. Gramse G, Kasper M, Fumigalli L, Gomila G, Hinterdorfer P, and Kienberger F, Nanotechnol. 26, 149501 (2014).

[28]. Chiara Biagi M, Fabregas R, Gramse G, Van Der Hofstadt M, Juárez A, Kienberger F, Fumigalli L, and Gomila G, ACS Nano 10, 280 (2016). [PubMed: 26643251]

[29]. Wang F, Clémet N, Ducatteau D, Troadec D, Tanbakuchi H, Legrand B, Dambrine G, and Théron D, Nanotechnol. (2014).

[30]. Huber HP, Moertelmaier M, Wallis TM, Chiang CJ, Hochleitner M, Imtiaz A, Oh YJ, Schilcher K, Dieudonne M, Smoliner J, Hinterdorfer P, Rosner SJ, Tanbakuchi H, Kabos P, and Kienberger F, Rev. Sci. Instrum 81, 113701 (2010). [PubMed: 21133472]

[31]. Brubaker MD, Levin I, Davydov AV, Rourke DM, Sanford NA, Bright VM, and Bertness KA, J. Appl. Phys 110, 053506 (2011).

[32]. Sanford NA, Robins LH, Blanchard PT, Soria K, Klein B, Eller BS, Bertness KA, Schlager JA, and Sanders AW, J. Appl. Phys 113, 174306 (2013).

[33]. Blanchard P, Bertness KA, Harvey T, and Sanford N, Semicond. Sci. Technol 29, 054005 (2014).

[34]. Lymperakis L, Weidlich PH, Eisele H, Schnedler M, Nys J-P, Grandidier B, Stivenard D, Dunin-Borkowski RE, Neugebauer J, and Ebert P, Appl. Phys. Lett 103, 152101 (2013).

[35]. Coakley KJ, Imtiaz A, Wallis TM, Weber JC, Berweger S, and Kabos P, Ultramicroscopy 150, 1 (2015). [PubMed: 25463325]

[36]. See supplementary material at [] for an expanded discussion of NW current hysteresis and tip current injection.
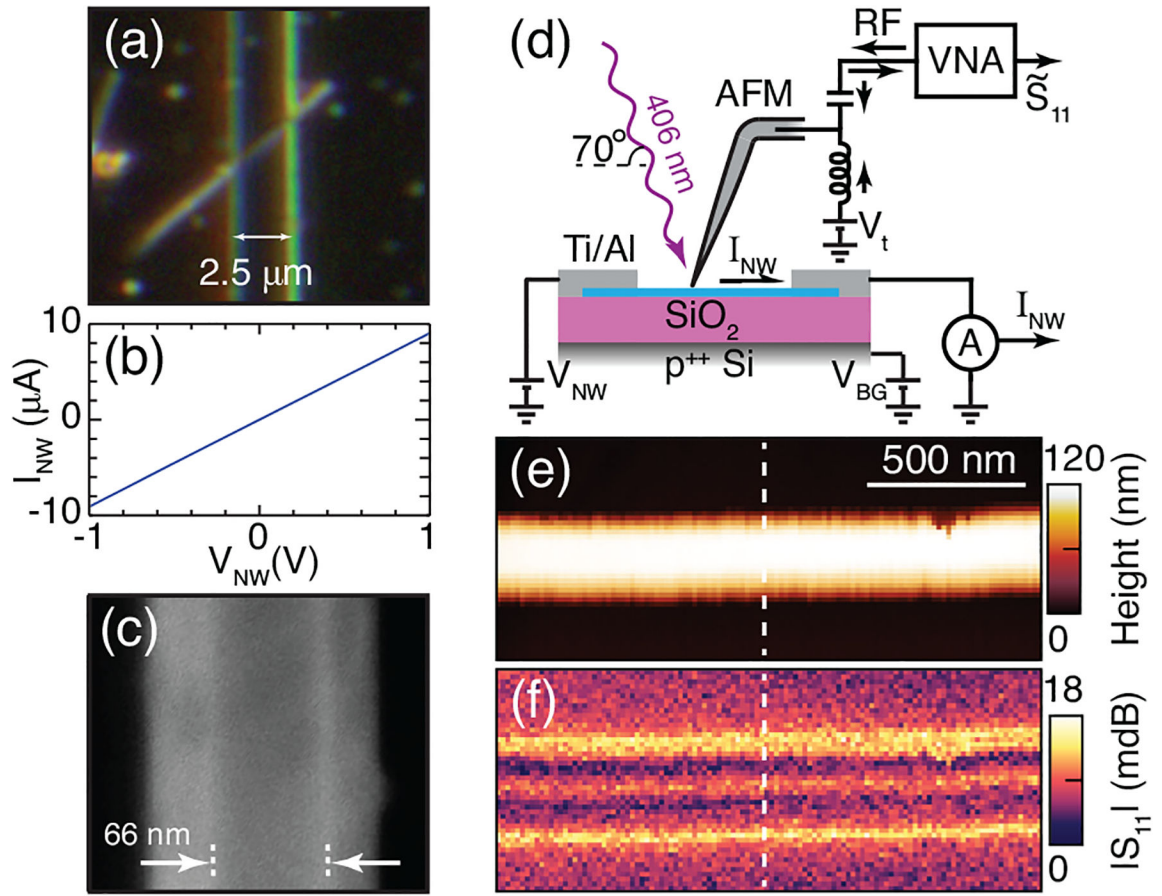
FIG. 1.

(a) Optical micrograph of NW device with a gap width of 2.5 μm. (b) *I-V* curve showing the ohmic NW device with dark resistance of ~100 kΩ (c) High-resolution SEM micrograph of NW showing hexagonal cross-section and top facet width of ~66 nm. (d) Schematic of experimental setup combining SMM with SGM. (e) Contact-mode AFM topography of the GaN NW studied here together with (f) the corresponding S_{11} signal magnitude.
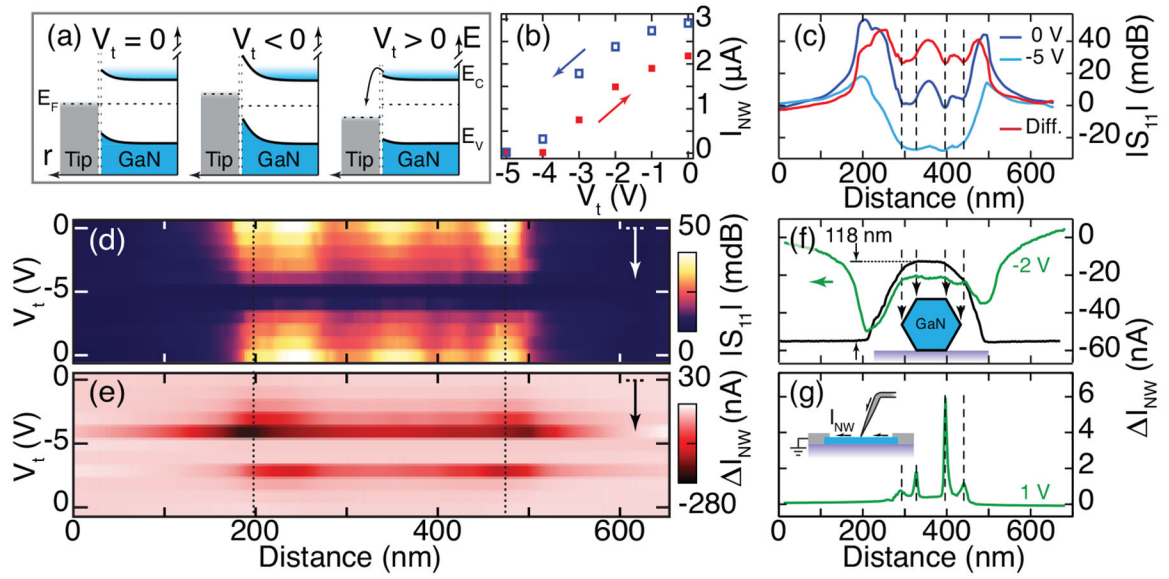
FIG. 2.

(a) Illustration of GaN surface band bending and the expected effect of the tip bias V_t on free carriers. (b) Absolute wire current with the tip at the center wire facet as a function of tip bias with increasing (blue open) and decreasing (red solid) bias magnitude as indicated by arrows. (c) SMM signal across the nanowire with intrinsic doping (blue), fully depleted (cyan), and the difference (red) showing the intrinsic free carrier contribution to the signal. (d) Bias-dependent free carrier contribution to the S_{11} signal and (e) corresponding change in NW current. (f) Line cuts of Contact-mode AFM topography and I for $V_t = -2$ V. (g) Spatial variations in I with $V_t = 1$ V.